

---

---

# Heterogeneity in Intratumor Correlations of $^{18}\text{F}$ -FDG, $^{18}\text{F}$ -FLT, and $^{61}\text{Cu}$ -ATSM PET in Canine Sinonasal Tumors

Tyler J. Bradshaw<sup>1</sup>, Stephen R. Bowen<sup>2</sup>, Ngonch Jallow<sup>1</sup>, Lisa J. Forrest<sup>3</sup>, and Robert Jeraj<sup>1,4</sup>

<sup>1</sup>Department of Medical Physics, School of Medicine and Public Health, University of Wisconsin, Madison, Wisconsin; <sup>2</sup>Departments of Radiation Oncology and Radiology, University of Washington, Seattle, Washington; <sup>3</sup>Department of Surgical Sciences, School of Veterinary Medicine, University of Wisconsin, Madison, Wisconsin; and <sup>4</sup>Department of Human Oncology, School of Medicine and Public Health, University of Wisconsin, Madison, Wisconsin

Intratumor heterogeneity in biologic properties and in relationships between various phenotypes may present a challenge for biologically targeted therapies. Understanding the relationships between different phenotypes in individual tumor types could help inform treatment selection. The goal of this study was to characterize spatial correlations of glucose metabolism, proliferation, and hypoxia in 2 histologic types of tumors. **Methods:** Twenty canine veterinary patients with spontaneously occurring sinonasal tumors (13 carcinomas and 7 sarcomas) were imaged with  $^{18}\text{F}$ -FDG,  $^{18}\text{F}$ -labeled 3'-deoxy-3'-fluorothymidine ( $^{18}\text{F}$ -FLT), and  $^{61}\text{Cu}$ -labeled diacetyl-bis(*N*<sup>4</sup>-methylthiosemicarbazone) ( $^{61}\text{Cu}$ -ATSM) PET/CT on 3 consecutive days. Precise positioning and immobilization techniques coupled with anesthesia enabled motionless scans with repeatable positioning. Standardized uptake values (SUVs) of gross sarcoma and carcinoma volumes were compared by use of Mann-Whitney *U* tests. Patient images were rigidly registered together, and intratumor tracer uptake distributions were compared. Voxel-based Spearman correlation coefficients were used to quantify intertracer correlations, and the correlation coefficients of sarcomas and carcinomas were compared. The relative overlap of the highest uptake volumes of the 3 tracers was quantified, and the values were compared for sarcomas and carcinomas. **Results:** Large degrees of heterogeneity in SUV measures and phenotype correlations were observed. Carcinoma and sarcoma tumors differed significantly in SUV measures, with carcinoma tumors having significantly higher  $^{18}\text{F}$ -FDG maximum SUVs than sarcoma tumors (11.1 vs. 5.0;  $P = 0.01$ ) as well as higher  $^{61}\text{Cu}$ -ATSM mean SUVs (2.6 vs. 1.2;  $P = 0.02$ ). Carcinomas had significantly higher population-averaged Spearman correlation coefficients than sarcomas in comparisons of  $^{18}\text{F}$ -FDG and  $^{18}\text{F}$ -FLT (0.80 vs. 0.61;  $P = 0.02$ ),  $^{18}\text{F}$ -FLT and  $^{61}\text{Cu}$ -ATSM (0.83 vs. 0.38;  $P < 0.0001$ ), and  $^{18}\text{F}$ -FDG and  $^{61}\text{Cu}$ -ATSM (0.82 vs. 0.69;  $P = 0.04$ ). Additionally, the highest uptake volumes of the 3 tracers had significantly greater overlap in carcinomas than in sarcomas. **Conclusion:** The relationships of glucose metabolism, proliferation, and hypoxia were heterogeneous across different tumors, with carcinomas tending to have high correlations and sarcomas having low correlations. Consequently, canine carcinoma tumors are robust targets for therapies that target a single biologic property, whereas sarcoma tumors may not be well suited for such therapies. Histology-specific PET correlations have far-reaching implications for the robustness of biologic target definition.

**Key Words:**  $^{18}\text{F}$ -FDG;  $^{61}\text{Cu}$ -ATSM;  $^{18}\text{F}$ -FLT; dose painting; heterogeneity

**J Nucl Med 2013; 54:1931–1937**

DOI: 10.2967/jnumed.113.121921

---

**T**wo types of biologic heterogeneity are often associated with malignant tumors: heterogeneity between tumors and heterogeneity within tumors. Biologic heterogeneity between tumors occurs when various degrees of biologic properties, such as oxygenation status or metastatic potential, are observed across different tumors; this heterogeneity causes variable clinical responses to standard-of-care therapies. Heterogeneity within tumors—or intratumor heterogeneity—occurs when a single tumor has regional variations in biologic—and even genetic—properties (*1*). Intratumor heterogeneity presents a challenge for advanced therapies in which specific biologic processes are targeted: certain tumor regions might express the biologic target, but other tumor regions might not. With increasing interest in therapies that target specific biologic mechanisms, measuring intratumor heterogeneity might help inform treatment selection and could influence staging and treatment response assessment. Functional imaging, such as PET, is a noninvasive method for determining how biologic properties are spatially distributed throughout a tumor.

Although measuring spatial patterns of a single phenotype within a tumor may help describe certain biologic aspects of the tumor, understanding the spatial relationships between different biologic properties provides greater insight into the underlying biologic status of the tumor. For example, Busk et al. found that the spatial concordance between tumor glucose metabolism and hypoxia varied with different histologic types of tumors, indicating that different histologic types of tumors have various degrees of dependence on aerobic glycolysis (*2*). Lohith et al. also found significant differences in the spatial relationships between glucose metabolism and hypoxia in lung adenocarcinoma and lung squamous cell carcinoma tumors, as assessed by PET (*3*). Understanding the spatial relationships between tumor phenotypes may help both researchers and clinicians in tasks such as biomarker development, therapy selection, and interpretation of responses to therapies.

Biologically conformal radiotherapy, or dose painting, is another area in which spatial concordance or discordance between different biologic properties within a tumor can have a large impact. In dose painting, a new paradigm in radiation therapy, a nonuniform dose is

---

Received Mar. 4, 2013; revision accepted Jun. 17, 2013.  
For correspondence or reprints contact: Robert Jeraj, University of Wisconsin–Madison, 1111 Highland Ave., Room 1005, Madison, WI 53705-2275.  
E-mail: rjeraj@wisc.edu  
Published online Sep. 16, 2013.  
COPYRIGHT © 2013 by the Society of Nuclear Medicine and Molecular Imaging, Inc.

tailored to match the spatial distribution of the biologic properties of a tumor (4). However, it is uncertain which biologic property should be targeted. Tumors in which different biologic targets (e.g., cellular hypoxia and glucose metabolism) have similar spatial distributions would be robust targets for dose painting: targeting a single phenotype would result in a similar treatment plan to targeting other phenotypes. However, in tumors in which different biologic targets cluster in different regions of the tumor, dose painting treatment plans would be sensitive to the choice of biologic target. Measuring spatial distributions of different biologic targets could help identify histologic types of tumors that are most likely to respond to dose painting treatments.

The purposes of this study were to measure and compare the spatial distributions of 3 biologic properties in tumors—glucose metabolism, cellular proliferation, and hypoxia—in 2 histologic types of tumors. Surrogates of these properties were measured with PET radiotracers  $^{18}\text{F}$ -FDG,  $^{18}\text{F}$ -labeled 3'-deoxy-3'-fluorothymidine ( $^{18}\text{F}$ -FLT), and  $^{61}\text{Cu}$ (II)-labeled diacetyl-bis( $N^4$ -methylthiosemicarbazone) ( $^{61}\text{Cu}$ -ATSM), respectively. Canine veterinary patients with spontaneously occurring carcinoma and sarcoma sinonasal tumors were imaged. These patients were ideal subjects for this study because we were able to eliminate motion during imaging, ensure repeatable positioning, and accurately register images. Furthermore, dogs are excellent models for understanding human cancers (5). We compared the  $^{18}\text{F}$ -FDG,  $^{18}\text{F}$ -FLT, and  $^{61}\text{Cu}$ -ATSM PET uptake patterns of canine sarcoma and carcinoma tumors; our experiments included a comparison of uptake magnitudes and an analysis of the spatial relationships of the 3 tracer distributions.

## MATERIALS AND METHODS

### Patient Population

Twenty canine patients of different breeds were included in the study. Companion animal (pet) dogs were referred to the University of Wisconsin Veterinary Medical Teaching Hospital. The research protocol was approved by the Animal Care and Use Committee of the University of Wisconsin, and all canine owners signed a written informed consent form. Patients were diagnosed with CT, and biopsies for histopathologic evaluation were obtained. All dogs had nasal or paranasal sinus tumors of stages 1–3 (mean tumor volume, 56 cm<sup>3</sup>), with no evidence of distant metastases or intracranial extension. Histopathologic evaluation revealed that 12 dogs had adenocarcinomas, 6 had chondrosarcomas, 1 had a squamous cell carcinoma, and 1 had an osteosarcoma. A veterinarian monitored all imaging sessions.

### Tracer Production

$^{61}\text{Cu}$  (half-life, 204.5 min) was produced via the  $^{60}\text{Ni}(d,n)^{61}\text{Cu}$  reaction at the University of Wisconsin cyclotron. The  $^{61}\text{Cu}$ -ATSM tracer was synthesized via the process outlined by Avila-Rodriguez (6). Analytic high-performance liquid chromatography of  $^{61}\text{Cu}$ -ATSM revealed a radiochemical purity of greater than 95% and typical specific activities of  $3.7 \times 10^{10}$ – $11.1 \times 10^{10}$  Bq/ $\mu\text{mol}$  (1–3 Ci/ $\mu\text{mol}$ ). The  $^{18}\text{F}$ -FLT tracer was also produced at the University of Wisconsin cyclotron, and the  $^{18}\text{F}$ -FDG tracer was provided by IBA Molecular.

### Imaging Procedure

Each canine patient underwent  $^{18}\text{F}$ -FDG,  $^{18}\text{F}$ -FLT, and  $^{61}\text{Cu}$ -ATSM PET/CT imaging on 3 consecutive days as part of a phase I/II clinical trial investigating dose painting. Scans were performed approximately 24 h apart.

The protocol for PET/CT imaging was as follows. Dogs fasted for at least 12 h before each scan. They were injected with 150–370 MBq (4–10 mCi) of tracer, depending on their size. After injection, the dogs

were kept in a kennel to limit physical activity. The dogs were anesthetized during scans with an initial propofol bolus injection and then isoflurane plus 100% oxygen. The time between tracer injection and the start of  $^{18}\text{F}$ -FDG PET scans was 60 min; for  $^{61}\text{Cu}$ -ATSM scans, the interval was 3 h.  $^{18}\text{F}$ -FLT scans were acquired dynamically. For reproducible positioning between PET/CT scans, the dogs' maxillae were positioned into custom dental molds fixed to the scanner couch, and their bodies were immobilized by vacuum mattresses (7).

All scans were performed on a Discovery VCT (GE Healthcare) PET/CT scanner.  $^{18}\text{F}$ -FDG and  $^{61}\text{Cu}$ -ATSM scans were 20-min 3-dimensional static acquisitions over a single 15-cm bed position.  $^{18}\text{F}$ -FLT scans were 90-min 3-dimensional dynamic acquisitions over a single 15-cm bed position. Emission data were attenuation-corrected and reconstructed with ordered-subset expectation maximization (2 iterations, 35 subsets, and 3-mm postfiltering). The image grid was  $256 \times 256 \times 47$ , with voxel sizes of  $2.0 \times 2.0 \times 3.3$  mm. Activity measurements were converted to standardized uptake values (SUVs) for analysis. For  $^{18}\text{F}$ -FLT scans, SUVs were calculated by averaging the frames from 60 to 90 min.

### Data Analysis

The magnitudes of  $^{18}\text{F}$ -FDG,  $^{18}\text{F}$ -FLT, and  $^{61}\text{Cu}$ -ATSM uptake in sarcoma ( $n = 7$ ) and carcinoma ( $n = 13$ ) tumors were compared. Veterinarians contoured gross tumor volumes (GTVs) on the basis of CT images. The maximum voxel SUV of the GTV ( $\text{SUV}_{\text{max}}$ ), the mean SUV of a 1-cm<sup>3</sup> sphere centered at the  $\text{SUV}_{\text{max}}$  ( $\text{SUV}_{\text{peak}}$ ), and the mean SUV of the GTV ( $\text{SUV}_{\text{mean}}$ ) were calculated for each canine patient. The  $\text{SUV}_{\text{max}}$ ,  $\text{SUV}_{\text{peak}}$ , and  $\text{SUV}_{\text{mean}}$  of sarcomas and carcinomas were then compared, and 2-sided Mann-Whitney  $U$  tests were used to determine significant differences. Tests of significance were robust to outliers in the distribution. In addition,  $F$  tests were used to compare the variances of SUV measures in sarcomas and carcinomas.

For each patient, all CT images were cropped to include only the volume of interest and then rigidly registered in Amira (Visage Imaging Inc.) to a single reference CT image by use of mutual information; the resulting transformations were applied to their respective PET data. This process allowed for a voxel-based comparison of  $^{18}\text{F}$ -FDG,  $^{18}\text{F}$ -FLT, and  $^{61}\text{Cu}$ -ATSM uptake distributions in each tumor. Voxel-based Spearman rank correlation coefficients were calculated for each tracer combination:  $^{18}\text{F}$ -FLT– $^{61}\text{Cu}$ -ATSM,  $^{18}\text{F}$ -FDG– $^{61}\text{Cu}$ -ATSM, and  $^{18}\text{F}$ -FDG– $^{18}\text{F}$ -FLT. Spearman rank correlation coefficients were used instead of Pearson correlation coefficients to avoid assumptions of linearity and normality. Correlation coefficients were averaged for sarcomas and carcinomas with the Fisher transformation, and 2-sided  $t$  tests were used to determine significant differences between the 2 tumor histology  $z$  score distributions.

In addition to the voxel-based analysis, tracer uptake patterns in sarcoma and carcinoma tumors were compared by analyzing the degrees of overlap of tracer-avid uptake regions. Tracer-avid volumes were created for each tracer by applying a threshold to each tracer's  $\text{SUV}_{\text{max}}$  within the GTV, resulting in 3 tracer-avid volumes per tumor. From these 3 volumes we calculated the percentage of overlap relative to the total threshold volume (i.e., the intersect relative to the union). Because the best threshold for segmenting tumor volumes is unknown, we applied several different thresholds, from 10% to 90% of the  $\text{SUV}_{\text{max}}$  in 10% increments. At each threshold level, the percentage of overlap was quantified. The overlap percentages were then averaged for both histologic types of tumors, and  $t$  tests were used to determine whether the degrees of overlap in the 2 histologic types of tumors were significantly different. To better visualize the histology-averaged tracer overlap, we created Venn diagrams (8) for each threshold level.

**TABLE 1**  
Histology-Averaged SUV Measures

Tracer	SUV <sub>mean</sub>			SUV <sub>max</sub>			SUV <sub>peak</sub>		
	Sarcomas	Carcinomas	<i>P</i>	Sarcomas	Carcinomas	<i>P</i>	Sarcomas	Carcinomas	<i>P</i>
<sup>18</sup> F-FDG	2.3	4.5	0.057	5.0	11.1	0.014	3.9	8.3	0.057
<sup>18</sup> F-FLT	1.3	2.7	0.38	2.8	7.6	0.13	1.9	5.3	0.27
<sup>61</sup> Cu-ATSM	1.2	2.6	0.022	4.6	7.4	0.15	3.3	5.5	0.13

## RESULTS

### Magnitude of Tracer Uptake

Table 1 shows SUV measures averaged for sarcomas and carcinomas, with *P* values resulting from Mann–Whitney *U* tests. Carcinomas had significantly higher <sup>18</sup>F-FDG SUV<sub>max</sub> than sarcomas (11.1 vs. 5.0; *P* = 0.01) as well as higher <sup>61</sup>Cu-ATSM SUV<sub>mean</sub> (2.6 vs. 1.2; *P* = 0.02). Differences in <sup>18</sup>F-FDG SUV<sub>mean</sub> and SUV<sub>peak</sub> approached significance (*P* = 0.057). For all SUV measures, carcinomas had higher average levels of uptake than sarcomas. Box plots of SUV<sub>mean</sub> and SUV<sub>max</sub> measurements are shown in Figure 1. It is evident from Figure 1 that the interpatient range, or variance, in SUV measures was much larger for carcinomas than for sarcomas. This finding was confirmed by *F* tests, which showed the variances in the 2 histologic types of tumors to be significantly different (*P* < 0.01) in all cases except the <sup>61</sup>Cu-ATSM SUV<sub>max</sub> and SUV<sub>mean</sub>. The average tumor volumes in the 2 histologic types of tumors were not significantly different.

### Spatial Correlations

Figure 2 shows voxel-based SUV scatterplots for 3 canine patients with carcinomas and 3 canine patients with sarcomas. For 4 of the 7 sarcoma tumors, the <sup>18</sup>F-FLT–<sup>61</sup>Cu-ATSM scatterplots appeared to be bifurcated, with one arm of low hypoxia and various degrees of proliferation and another arm with low proliferation and various degrees of hypoxia. For the other 3 sarcoma tumors, the scatterplots were fan-shaped. On the other hand, for carcinoma tumors, correlations between phenotypes were generally high. Box plots of voxel-based Spearman correlation coefficients, separated by histologic types of tumors, are shown in Figure 3. Fisher-averaged correlation coefficients and *t* test results are shown in Table 2. Carcinomas had significantly higher intertracer

correlations than sarcomas for all tracer comparisons. The greatest differences between the 2 histologic types of tumors were observed for the <sup>18</sup>F-FLT–<sup>61</sup>Cu-ATSM correlations: the average correlation coefficients were 0.38 for sarcomas and 0.83 for carcinomas (*P* < 10<sup>−4</sup>).

### Overlapping Volumes

Examples of tracer-avid volumes at a 70% threshold are shown for 12 tumors in Figure 4. Tracer-avid regions generally overlapped in carcinoma tumors but were spatially separated in sarcoma tumors. Figure 5 shows Venn diagram representations of inter-tracer overlap, averaged for carcinomas and sarcomas, at 9 SUV thresholds. For low thresholds (≤30%) and high thresholds (90%), no significant differences between the 2 histologic types of tumors were observed. However, for thresholds between 40% and 80%, significant differences between sarcomas and carcinomas were observed; *t* test results are shown in Table 3. No significant differences between sarcomas and carcinomas were observed for <sup>18</sup>F-FDG–<sup>18</sup>F-FLT overlap at any threshold. For <sup>61</sup>Cu-ATSM–<sup>18</sup>F-FDG and <sup>61</sup>Cu-ATSM–<sup>18</sup>F-FLT overlap, differences between sarcomas and carcinomas were significant at thresholds of 40%–80%, with carcinomas having greater average overlap. The regions in which all 3 tracers overlapped were also significantly larger in carcinomas at thresholds of 40%–70%.

## DISCUSSION

In comparing <sup>18</sup>F-FDG, <sup>18</sup>F-FLT, and <sup>61</sup>Cu-ATSM uptake patterns in canine nasal tumors, we found that sarcoma tumors had significantly lower levels of <sup>18</sup>F-FDG and <sup>61</sup>Cu-ATSM uptake than carcinoma tumors. Two other studies—1 in dogs (9) and 1 in human lung cancer patients (10)—compared <sup>18</sup>F-FDG uptake in

sarcoma and carcinoma tumors and found similar results. Lower levels of <sup>18</sup>F-FDG and <sup>61</sup>Cu-ATSM uptake may be indicative of a less aggressive phenotype in sarcoma tumors and may partly explain why patients with sarcomas respond better to treatment (11). However, low levels of uptake may also be caused by a lower tumor cell density or poor vascularity, which are characteristic of chondrosarcoma tumors (12).

The present study was unique in its ability to establish accurate voxelwise phenotype correlations. As registration inaccuracies can significantly degrade voxelwise correlations between images (13), canine nasal tumors were chosen for the present study because the nondeformable bony anatomy surrounding the nasal cavity enables accurate image registration, mitigating such

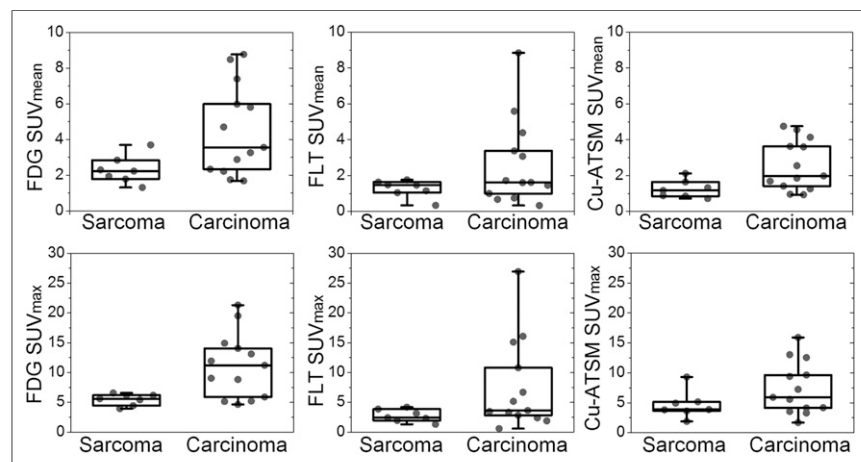


**FIGURE 1.** Quartile box plots representing distributions of SUV<sub>mean</sub> and SUV<sub>max</sub> for <sup>18</sup>F-FDG, <sup>18</sup>F-FLT, and <sup>61</sup>Cu-ATSM PET scans, separated by tumor histology.

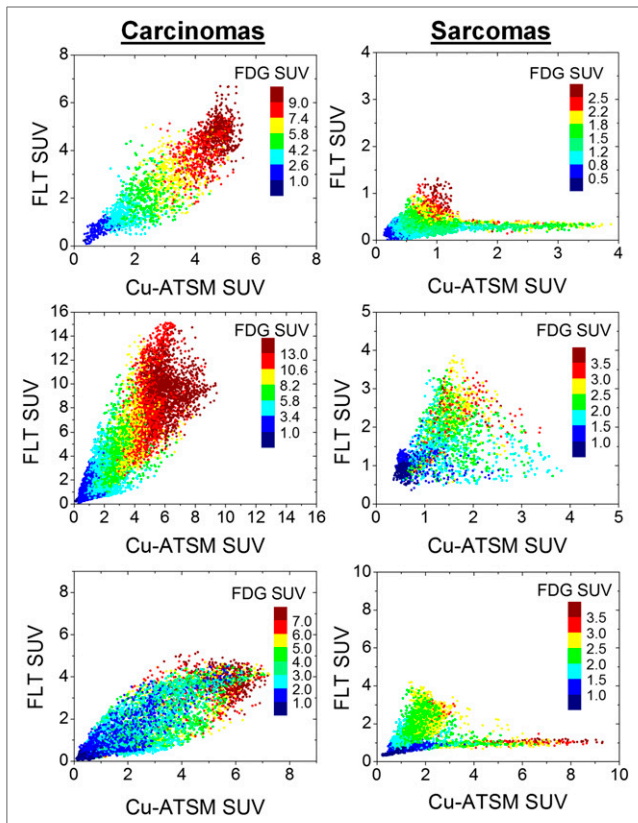


**FIGURE 2.** Voxel-based SUV scatter plots for 3 canine patients with carcinomas and 3 canine patients with sarcomas, illustrating intratumor tracer correlations. Each point represents voxel inside tumor; position and color represent voxel's SUVs from 3 PET scans.

errors. Motion blurring can also make image comparison difficult by smoothing out heterogeneities and causing images to appear similar (14). However, because canine patients experienced no motion during scans as a result of anesthesia, differences between images were apparent, as was notably observed in patients with sarcomas. In addition, tumors were large enough to provide significant intratumor heterogeneity. Because scans were obtained on consecutive days, uncertainties associated with tumor deformation and cellular redistribution were minimal. These precisely controlled conditions allowed for an accurate assessment of phenotype correlations, which might not be reproducible in human studies.

Spatial correlations of  $^{18}\text{F}$ -FDG,  $^{18}\text{F}$ -FLT, and  $^{61}\text{Cu}$ -ATSM PET were heterogeneous across canine patients, with Spearman correlation

**TABLE 2**  
Histology-Averaged Spearman Correlation Coefficients

Tracer combination	Average $\rho$ for:		<i>P</i>
	Sarcomas	Carcinomas	
$^{18}\text{F}$ -FLT- $^{61}\text{Cu}$ -ATSM	0.38	0.83	<0.0001
$^{18}\text{F}$ -FDG- $^{61}\text{Cu}$ -ATSM	0.69	0.82	0.04
$^{18}\text{F}$ -FDG- $^{18}\text{F}$ -FLT	0.61	0.80	0.02

coefficients ranging from 0.14 to 0.98. Carcinoma tumors had significantly higher correlations and levels of colocalization of tracers than sarcoma tumors. The greatest discordance between the 2 histologic types of tumors was noted for the  $^{18}\text{F}$ -FLT- $^{61}\text{Cu}$ -ATSM correlations. In 4 of the 7 patients with sarcomas, there were distinctive bifurcations in the  $^{18}\text{F}$ -FLT- $^{61}\text{Cu}$ -ATSM scatterplots (3 of these patients also had minor bifurcations in the  $^{18}\text{F}$ -FDG- $^{61}\text{Cu}$ -ATSM scatterplots), which have not been reported in the literature. The 2 branches, when mapped back into 3-dimensional image space, resulted in 2 spatially contiguous tumor regions. This finding suggests that significant phenotypic heterogeneity exists in sarcoma tumors, with distinct regions of proliferation, distinct regions of hypoxia, and various levels of metabolism.

The biologic underpinnings of the observed uptake patterns are unclear but may be related to different cellular responses to hypoxia. Assuming that high levels of  $^{18}\text{F}$ -FDG,  $^{18}\text{F}$ -FLT, and  $^{61}\text{Cu}$ -ATSM uptake indicate the colocalization of metabolism, proliferation, and hypoxia, the high intertracer correlations observed in carcinomas may be explained by increased cellular hypoxia-inducible factor 1 activity, which can activate metabolic enzymes and transporters and drive proliferation (15). This reasoning may be supported by a study by Kaira et al., who reported that human lung carcinoma patients had significantly higher levels of hypoxia-inducible factor 1 $\alpha$  expression than lung sarcoma patients (10). Conversely, the low intertracer correlations observed in sarcomas may be due to a preference of sarcoma cells to undergo cell cycle arrest under hypoxic conditions, thereby lowering proliferation rates (16). However, because the SUV of a voxel reflects only an average of the many cellular processes occurring within its macroscopic volume, we cannot explain the trends with certainty. Interestingly, although sarcoma tumors had significantly more phenotypic heterogeneity than carcinoma tumors, canine nasal sarcoma tumors were reported to respond better to treatment than carcinoma tumors (11). In contrast, other studies showed that intratumor heterogeneity, although defined and measured differently, was associated with a poorer outcome (17).

Treatments designed to specifically target certain tumor phenotypes (e.g., dose painting) may result in different outcomes for carcinoma and sarcoma tumors. In carcinomas, in which proliferative, hypoxic, and metabolic phenotypes were colocalized, targeting a single phenotype would likely simultaneously target the other 2 phenotypes. Alternatively, in sarcomas, each tracer accumulated in different regions of the tumor, and targeting a single phenotype would likely miss tumor regions with high levels of expression of the other 2 phenotypes. It is also possible that in different histologic

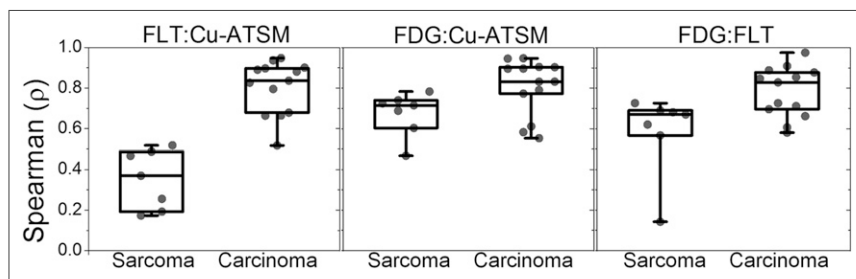


**FIGURE 3.** Quartile box plots representing distributions of voxel-based Spearman correlation coefficients for comparisons of  $^{18}\text{F}$ -FLT and  $^{61}\text{Cu}$ -ATSM,  $^{18}\text{F}$ -FDG and  $^{61}\text{Cu}$ -ATSM, and  $^{18}\text{F}$ -FDG and  $^{18}\text{F}$ -FLT in canine patients with sarcomas and carcinomas.

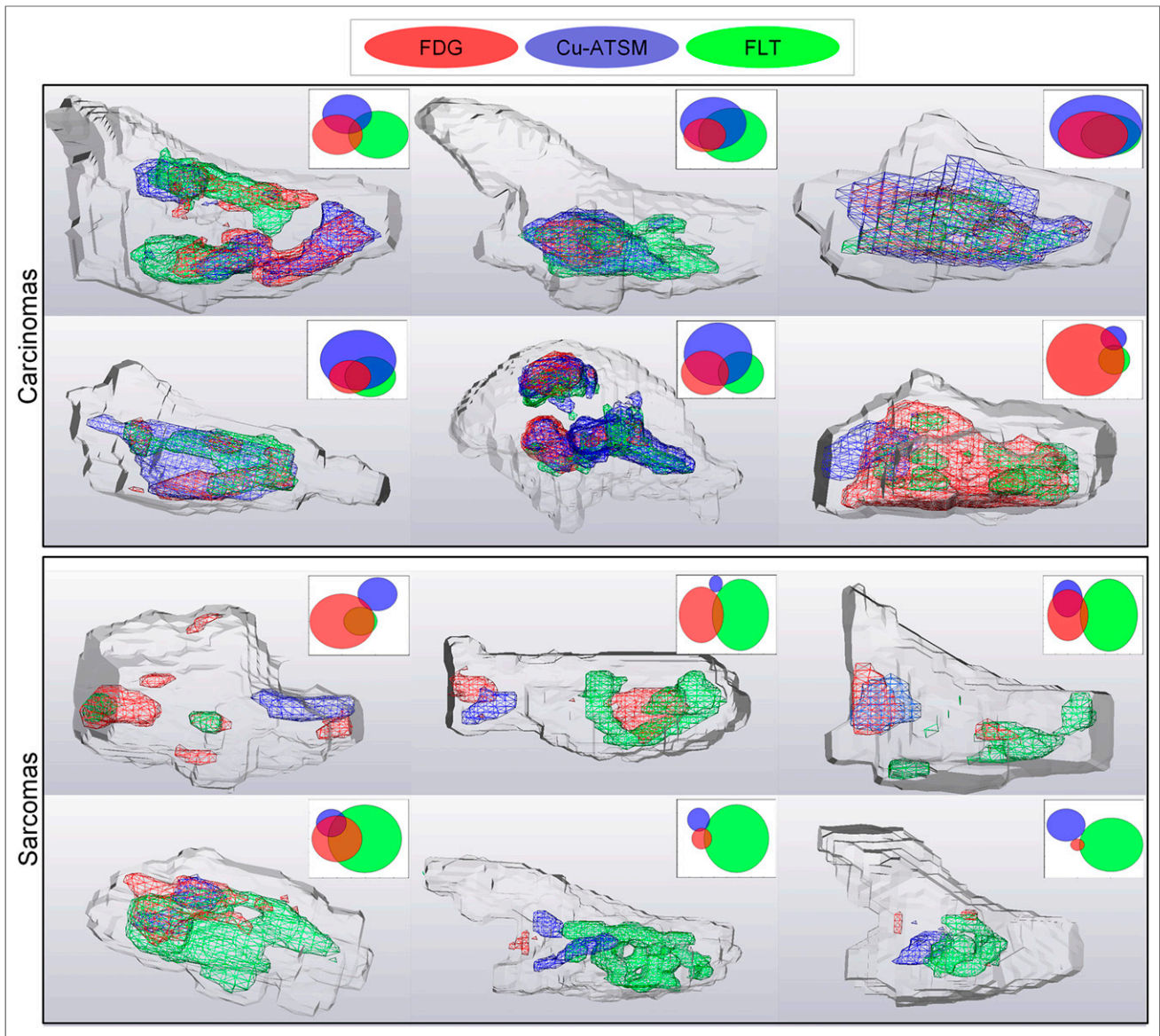


**FIGURE 4.** Three-dimensional representations of GTVs (gray outline) with tracer-avid volumes inside for 12 canine patients. Tracer-avid volumes presented in these images were created by applying 70% threshold to each tracer. Venn diagrams in upper right corners help visualize degree of overlap.

types of tumors, the relationships between various biologic properties and treatment resistance may be different. The latter was observed in a study involving a smaller subset of our patient population, in which we observed histology dependence when associating

distributions of different pretreatment tracers with follow-up  $^{18}\text{F}$ -FDG distributions (18).

The present study is the first study to report comparisons of 3 tracer distributions in 2 histologic types of tumors. Results from previous studies comparing 2 tracers in 2 or more histologic types of tumors were in agreement with our results—namely, that spatial correlations of different biologic properties are histology-specific (2,3,19). Tumor types with poor correlations between metabolic activity and hypoxia include colon adenocarcinomas (20) and Lewis lung carcinomas (21) in rodents and lung squamous cell carcinomas (3) and sarcomas (19) in humans. On the other hand, high correlations have been found in patients

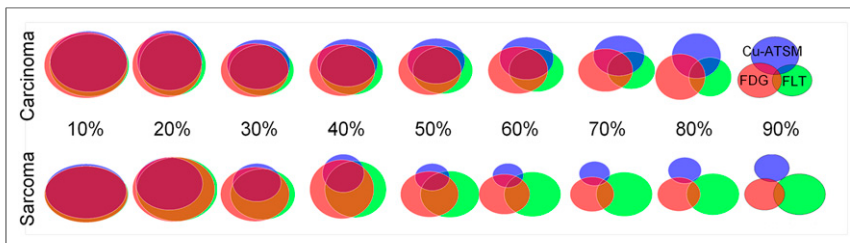


**FIGURE 5.** Venn diagrams representing average degrees of overlap of tracer-avid volumes at various thresholds, averaged for carcinomas and sarcomas.

**TABLE 3**  
Comparison of Overlapping Tracer-Avid Volumes  
for Sarcomas and Carcinomas

Region of overlap	P values for thresholds of:				
	40%	50%	60%	70%	80%
<sup>18</sup> F-FLT- <sup>61</sup> Cu-ATSM	0.02	<0.001	<0.001	0.004	0.04
<sup>18</sup> F-FDG- <sup>61</sup> Cu-ATSM	0.05	0.004	0.002	0.006	0.03
<sup>18</sup> F-FDG- <sup>18</sup> F-FLT					
<sup>18</sup> F-FLT- <sup>18</sup> F-FDG- <sup>61</sup> Cu-ATSM	0.04	0.002	0.001	0.002	

P values of greater than 0.05 are not shown. Significant values indicate that carcinomas had significantly greater overlap of respective tracers than sarcomas.

with head and neck cancers (19) and lung adenocarcinomas (3). Hansen et al. compared <sup>18</sup>F-FDG and <sup>61</sup>Cu-ATSM distributions in 6 sarcoma and 3 carcinoma canine tumors and found moderate to strong voxel-based correlations but reported no comparisons of histologic types of tumors (22). In studies of <sup>18</sup>F-FLT and hypoxia correlations in tumors, various degrees of correlation were found in human oropharyngeal tumors (14), high correlations were found in a 9L gliosarcoma rat model (23), and low correlations were found in non-small cell lung cancer xenografts in mice (24). For intratumor correlations of <sup>18</sup>F-FDG and <sup>18</sup>F-FLT, McCall et al. reported high correlations in oropharyngeal tumors (13), whereas Huang et al. reported low levels of <sup>18</sup>F-FDG-<sup>18</sup>F-FLT overlap in non-small cell lung cancer xenografts (24). In other studies, <sup>18</sup>F-FDG uptake was found to be strongly influenced by the proliferation rate (25). Coupled with our findings, these reports suggest that in different histologic types of tumors, the relationships of biologic properties are substantially different—although trends do appear to occur within individual histologic types.

In the analysis of overlapping volumes, thresholds of 90% and less than or equal to 30% did not result in significantly different degrees of overlap of the histologic types of tumors. This finding was an expected consequence of the use of SUV thresholds: high SUV thresholds result in very small volumes and therefore very little overlap of tracer-avid volumes; low thresholds create tracer-avid volumes that encompass most of the GTV, resulting in almost complete overlap. An additional drawback to the use of thresholds is their sensitivity to the SUV<sub>max</sub>, which can be highly variable because of SUV uncertainties (26). On the other hand, voxel-based correlation coefficients are insensitive to the SUV<sub>max</sub> but can be sensitive to registration, noise, and the reconstruction algorithm used (13).

There are uncertainties in the interpretations of the results of the present study, particularly for application to human cancers. Although humans and dogs have many biologic similarities—they are more similar in growth rate, vasculature, treatment response, and gene expression profile than humans and mice (5)—the use of anesthesia and 100% O<sub>2</sub> during imaging may affect tracer uptake (27,28). <sup>61</sup>Cu-ATSM also has a lower binding affinity for serum albumin in dogs than in humans, potentially influencing uptake (29). Furthermore, we grouped together all sarcoma tumors (6 chondrosarcomas and 1 osteosarcoma) and all carcinoma tumors (12 adenocarcinomas and 1 squamous cell carcinoma) for analysis because of their similarities in tracer uptake patterns. However, we recognize that genetic profiles

can vary drastically in different sarcomas and carcinoma subtypes (30); therefore, phenotypic patterns may show different trends for different subtypes. Finally, there is uncertainty about the specificity of <sup>61</sup>Cu-ATSM for hypoxia. Understanding of the mechanism of <sup>61</sup>Cu-ATSM uptake has evolved over time (31), but this uptake was recently shown to be caused by impaired mitochondrial electron transport chain function—a consequence of cellular hypoxia (32). Nonetheless, some studies have reported cell line dependence in the specificity of <sup>61</sup>Cu-ATSM for hypoxia (33). Likewise, for <sup>18</sup>F-FDG and <sup>18</sup>F-FLT uptake, no tracer is a perfect surrogate for a single biologic process: tracer uptake is influenced by confounding factors, such as cellular density and vascularity.

## CONCLUSION

Using <sup>61</sup>Cu-ATSM, <sup>18</sup>F-FLT, and <sup>18</sup>F-FDG PET imaging, we have shown that the interrelationships of hypoxia, proliferation, and metabolism are significantly different in canine sarcoma and carcinoma tumors. The findings suggest that intratumor phenotypic heterogeneity can vary significantly across different histologic types of tumors. Consequently, therapies that target a single biologic process may result in different outcomes for different histologic types of tumors.

## DISCLOSURE

The costs of publication of this article were defrayed in part by the payment of page charges. Therefore, and solely to indicate this fact, this article is hereby marked “advertisement” in accordance with 18 USC section 1734. This work was funded by NIH grant R01 CA136927. No potential conflict of interest relevant to this article was reported.

## ACKNOWLEDGMENTS

We thank veterinary oncologist Lyndsay Kubicek for overseeing the imaging sessions and for her help in coordinating the study. We also thank members of the UW Image-Guided Therapy Group and the Veterinary Medical Teaching Hospital who assisted during PET/CT imaging and members of the UW Cyclotron Research Group for providing <sup>18</sup>F-FLT and <sup>61</sup>Cu-ATSM.

## REFERENCES

- Gerlinger M, Rowan AJ, Horswell S, et al. Intratumor heterogeneity and branched evolution revealed by multiregion sequencing. *N Engl J Med*. 2012;366:883–892.
- Busk M, Horsman MR, Kristjansen PEG, van der Kogel AJ, Bussink J, Overgaard J. Aerobic glycolysis in cancers: implications for the usability of oxygen-responsive genes and fluorodeoxyglucose-PET as markers of tissue hypoxia. *Int J Cancer*. 2008;122:2726–2734.
- Lohith TG, Kudo T, Demura Y, et al. Pathophysiologic correlation between <sup>62</sup>Cu-ATSM and <sup>18</sup>F-FDG in lung cancer. *J Nucl Med*. 2009;50:1948–1953.
- Ling CC, Humm J, Larson S, et al. Towards multidimensional radiotherapy (MD-CRT): biological imaging and biological conformality. *Int J Radiat Oncol Biol Phys*. 2000;47:551–560.
- Hansen K, Khanna C. Spontaneous and genetically engineered animal models; use in preclinical cancer drug development. *Eur J Cancer*. 2004;40:858–880.
- Avila-Rodriguez M. *Low Energy Cyclotron Production of Multivalent Transition Metals for PET Imaging and Therapy* [Ph.D. thesis]. Madison, WI: Medical Physics, University of Wisconsin; 2007.
- Kubicek LN, Seo S, Chappell RJ, Jeraj R, Forrest LJ. Helical tomotherapy setup variations in canine nasal tumor patients immobilized with a bite block. *Vet Radiol Ultrasound*. 2012;53:474–481.
- MATLAB Central File Exchange. *venn* [computer program]. <http://www.mathworks.com/matlabcentral/fileexchange/22282-venn>. Published November 20, 2008. Updated February 14, 2011. Accessed August 26, 2013.

9. Hansen AE, McEvoy F, Engelholm SA, Law I, Kristensen AT. FDG PET/CT imaging in canine cancer patients. *Vet Radiol Ultrasound*. 2011;52:201–206.
10. Kaira K, Okumura T, Ohde Y, et al. Correlation between <sup>18</sup>F-FDG uptake on PET and molecular biology in metastatic pulmonary tumors. *J Nucl Med*. 2011;52:705–711.
11. Kondo Y, Matsunaga S, Mochizuki M, et al. Prognosis of canine patients with nasal tumors according to modified clinical stages based on computed tomography: a retrospective study. *J Vet Med Sci*. 2008;70:207–212.
12. Gelderblom H, Hogendoorn PCW, Dijkstra SD, et al. The clinical approach towards chondrosarcoma. *Oncologist*. 2008;13:320–329.
13. Nyflot MJ, Harari PM, Yip S, Perlman SB, Jeraj R. Correlation of PET images of metabolism, proliferation and hypoxia to characterize tumor phenotype in patients with cancer of the oropharynx. *Radiother Oncol*. 2012;105:36–40.
14. McCall KC, Barbee DL, Kissick MW, Jeraj R. PET imaging for the quantification of biologically heterogeneous tumours: measuring the effect of relative position on image-based quantification of dose-painting targets. *Phys Med Biol*. 2010;55:2789–2806.
15. Vaupel P. The role of hypoxia-induced factors in tumor progression. *Oncologist*. 2004;9(suppl 5):10–17.
16. Gardner LB, Li Q, Park MS, Flanagan WM, Semenza GL, Dang CV. Hypoxia inhibits G1/S transition through regulation of p27 expression. *J Biol Chem*. 2001;276:7919–7926.
17. Eary JF, O'Sullivan F, O'Sullivan J, Conrad EU. Spatial heterogeneity in sarcoma <sup>18</sup>F-FDG uptake as a predictor of patient outcome. *J Nucl Med*. 2008;49:1973–1979.
18. Bowen SR, Chappell RJ, Bentzen SM, Deveau MA, Forrest LJ, Jeraj R. Spatially resolved regression analysis of pre-treatment FDG, FLT and Cu-ATSM PET from post-treatment FDG PET: an exploratory study. *Radiother Oncol*. 2012;105:41–48.
19. Rajendran JG, Mankoff DA, O'Sullivan F, et al. Hypoxia and glucose metabolism in malignant tumors: evaluation by [<sup>18</sup>F]fluoromisonidazole and [<sup>18</sup>F]fluorodeoxyglucose positron emission tomography imaging. *Clin Cancer Res*. 2004;10:2245–2252.
20. Yoshii Y, Furukawa T, Kiyono Y, et al. Copper-64-diacetyl-bis (N<sup>4</sup>-methylthiosemicarbazone) accumulates in rich regions of CD133+ highly tumorigenic cells in mouse colon carcinoma. *Nucl Med Biol*. 2010;37:395–404.
21. Oh M, Tanaka T, Kobayashi M, et al. Radio-copper-labeled Cu-ATSM: an indicator of quiescent but clonogenic cells under mild hypoxia in a Lewis lung carcinoma model. *Nucl Med Biol*. 2009;36:419–426.
22. Hansen AE, Kristensen AT, Law I, McEvoy FJ, Kjær A, Engelholm SA. Multimodality functional imaging of spontaneous canine tumors using <sup>64</sup>Cu-ATSM and <sup>18</sup>F-FDG PET/CT and dynamic contrast enhanced perfusion CT. *Radiother Oncol*. 2012;102:424–428.
23. Dence CS, Ponde DE, Welch MJ, Lewis JS. Autoradiographic and small-animal PET comparisons between <sup>18</sup>F-FMISO, <sup>18</sup>F-FDG, <sup>18</sup>F-FLT and the hypoxic selective <sup>64</sup>Cu-ATSM in a rodent model of cancer. *Nucl Med Biol*. 2008;35:713–720.
24. Huang T, Civelek AC, Li J, et al. Tumor microenvironment-dependent <sup>18</sup>F-FDG, <sup>18</sup>F-fluorothymidine, and <sup>18</sup>F-misonidazole uptake: a pilot study in mouse models of human non-small cell lung cancer. *J Nucl Med*. 2012;53:1262–1268.
25. Yamada K, Brink I, Bissé E, Epting T, Engelhardt R. Factors influencing [F-18] 2-fluoro-2-deoxy-D-glucose (F-18 FDG) uptake in melanoma cells: the role of proliferation rate, viability, glucose transporter expression and hexokinase activity. *J Dermatol*. 2005;32:316–334.
26. Kinahan PE, Fletcher JW. Positron emission tomography-computed tomography standardized uptake values in clinical practice and assessing response to therapy. *Semin Ultrasound CT MR*. 2010;31:496–505.
27. Fuchs K, Kukuk D, Reischl G, et al. Oxygen breathing affects 3'-deoxy-3'-<sup>18</sup>F-fluorothymidine uptake in mouse models of arthritis and cancer. *J Nucl Med*. 2012;53:823–830.
28. Kersemans V, Cornelissen B, Hueting R, et al. Hypoxia imaging using PET and SPECT: the effects of anesthetic and carrier gas on [Cu]-ATSM, [Tc]-HL91 and [F]-FMISO tumor hypoxia accumulation. *PLoS One*. 2011;6:e25911.
29. Basken NE, Green MA. Cu(II) bis(thiosemicarbazone) radiopharmaceutical binding to serum albumin: further definition of species dependence and associated substituent effects. *Nucl Med Biol*. 2009;36:495–504.
30. Baird K, Davis S, Antonescu CR, et al. Gene expression profiling of human sarcomas: insights into sarcoma biology. *Cancer Res*. 2005;65:9226–9235.
31. Dilworth JR, Hueting R. Metal complexes of thiosemicarbazones for imaging and therapy. *Inorganica Chim Acta*. 2012;389:3–15.
32. Donnelly PS, Liddell JR, Lim S, et al. An impaired mitochondrial electron transport chain increases retention of the hypoxia imaging agent diacetyl-bis(4-methylthiosemicarbazonato)copper(II). *Proc Natl Acad Sci USA*. 2012;109:47–52.
33. Yuan H, Schroeder T, Bowsler JE, Hedlund LW, Wong T, Dewhirst MW. Intertumoral differences in hypoxia selectivity of the PET imaging agent <sup>64</sup>Cu(II)-diacetyl-bis(N<sup>4</sup>-methylthiosemicarbazone). *J Nucl Med*. 2006;47:989–998.